

Experimental and Dimensional Analysis of Planar Flow Melt Spinning Process



Sowjanya Madireddi

Nomenclature

C_p	Specific heat J/kgK
G	Nozzle-wheel gap mm
h	Convective heat transfer coefficient W/m ² K
k	Thermal conductivity W/mk
l	Length of the nozzle mm
P	Pressure kPa
Pr	Prandtl number
R_a	Surface roughness μm
Re	Reynolds number
t	Ribbon thickness μm
T	Ejection temperature °C
T_g	Glass transition temperature K
U	Wheel speed m/s
w	Nozzle-slit width mm
μ	Viscosity Pa.s
δ_{Tx}	Thickness of thermal boundary layer
x	Distance from slit center mm

S. Madireddi (✉)
CVR College of Engineering, Hyderabad 501510, India
e-mail: madireddisowjanya@gmail.com

© The Author(s), under exclusive license to Springer Nature Singapore Pte Ltd. 2023
B. Bhattacharyya et al. (eds.), *Advances in Micro and Nano Manufacturing and Surface Engineering*, Lecture Notes in Mechanical Engineering,
https://doi.org/10.1007/978-981-19-4571-7_8

1 Introduction

Core losses in the distribution transformer attribute to the material structure (amorphous/crystalline) and thickness of the lamina. Eddy current losses are directly proportional to the thickness of the lamina, and hysteresis losses depend on the structure of the material. Good quality amorphous ribbons produced by planar flow melt spinning process (PFMS) reduce these losses by 75% if used as core material. Hence, the present work focuses on the analysis and prediction of the conditions to obtain a higher quality ribbon during PFMS process for $\text{Fe}_{73.5}\text{Nb}_3\text{Cu}_1\text{Si}_{13.5}\text{B}_9$ alloy. As many investigators presented work on different materials and process conditions, the process is generalized using dimensional analysis for any material-parameter combination.

Some experimental studies reported earlier considered the effect of process conditions on the thickness of the ribbons. Some investigators focused on obtaining improved soft magnetic properties in the ribbon and some others reported various topographies of the ribbons and few others on numerical models [9]. Investigators [12] performed a parametric study of the effect of process variables on ribbon thickness for Pb–Sn ribbons and defined a process window for this material. Thickness of the ribbons with jetting temperature was observed to [7] decrease due to viscosity, which may also vary with alloy composition. Carpenter et al. [3] presented ribbons with various surface defects, viz. dimple, streak and herringbone obtained during PFMS process at various process conditions. Heat transfer between cooling wheel and melt puddle influences the ribbon formation [17, 23], and quench rates [21] influence the crystallization of $\text{Fe}_{73.5}\text{Nb}_3\text{Cu}_1\text{Si}_{13.5}\text{B}_9$ alloy. Matsuki et al. [10] observed a decrease in iron and hysteresis losses of Fe-Si-B alloy ribbons with decrease in surface roughness. Szewieczek et al. [19] studied the corrosion properties of Metglas alloy at various conditions. They also studied its effect on the magnetic properties of Finemet alloy and found that surface roughness [20] of the ribbons greatly influences these properties. Wu et al. [22] observed air entrainment and formation of air pockets affecting the magnetic properties of the ribbons. Induced air pockets were observed on the wheel side of the ribbon while casting in air, whereas these pockets were absent during the vacuum casting of $\text{Ni}_{78}\text{Si}_8\text{B}_{14}$ ribbons. Cox et al. [4] reported the herringbone defect due to translator motion of the cooling wheel. Byrne et al. [1, 2] observed cross-wave defect due to vibration of the puddle. All of the investigations differ with each other in terms of material or process condition. This makes it difficult to apply and use the results obtained by one investigator directly by the other investigator.

The present work compares thickness, surface roughness, topography and amorphous structure of the ribbons obtained at various process conditions. The equations hence obtained through non-dimensionalization (dimensional analysis) will be useful for the experimentalists to predict the variation in thickness and surface roughness of the product at a given process condition for any material-parameter combination prior to experiment. Thereby, reduce the cost of experimental investigation to

predict optimum condition to produce higher quality ribbons for the existing or new materials.

2 Experimental

Finemet alloy ($\text{Fe}_{73.5}\text{Si}_{13.5}\text{B}_9\text{Nb}_3\text{Cu}_1$) which possesses ultra-soft magnetic properties was used for the experimentation. Crucibles made of quartz having rectangular slit with length (l) and width (w) and with circular lobes at the end were employed to hold the material for induction heating. Material samples of approx. 150–200 g were used for each experiment. The sample was melted in the crucible using an induction heater. The crucible was brought down to the preset nozzle-wheel gap (G) when the melt reached to the required temperature (T). The melt was ejected by applying inert gas pressure (P) on to a rotating cooling wheel at a set speed (U). Solidified melt in the form of a ribbon was ejected from the under cooled puddle due to wheel rotation. Figure 1a shows the schematic of the puddle formation and ejection of ribbon from the under cooled puddle. USM and DSM represent upstream and downstream meniscus, respectively. Table 1 gives the process conditions at which parametric study was performed using Finemet alloy $\text{Fe}_{73.5}\text{Si}_{13.5}\text{B}_9\text{Nb}_3\text{Cu}_1$. Thickness and surface roughness were measured, and XRD analysis was performed on the as-spun ribbons.

3 Results and Discussion

The melt, which comes out through the rectangular slit upon ejection by gas pressure, accumulates in the form of a puddle in the nozzle-wheel gap. Heat transfer from the melt to the cooling wheel initiates the rapid solidification (freezing) of melt at its glass transition temperature T_g (point A) as shown in Fig. 1a. The thickness of the solidified material grows in the puddle until the downstream meniscus (DSM). The intersection point of solidified material, molten alloy and DSM (Fig. 1a, point B) determines the ribbon thickness. The condition of the melt at this point influences the surface quality of the ribbon.

In the present work, the reasons for the surface quality of the ribbon at various process conditions are analyzed for the first time using the boundary layer theory. For liquid metal flows, thickness of thermal boundary layer is higher than that of velocity boundary layer. As the melt solidifies at T_g and comes out of the puddle at point B (Fig. 1a), thickness of the ribbon can be assumed as the thickness of thermal boundary layer at T_g of the alloy. On the other hand, the laminar or turbulent flow condition of the melt at point B can be predicted using the non-dimensional form of velocity represented by Reynolds number for various process conditions. As the flow of melt depends on velocity and viscosity, calculation of Reynolds number (ratio of inertia to viscous forces) helps to analyze the surface quality.

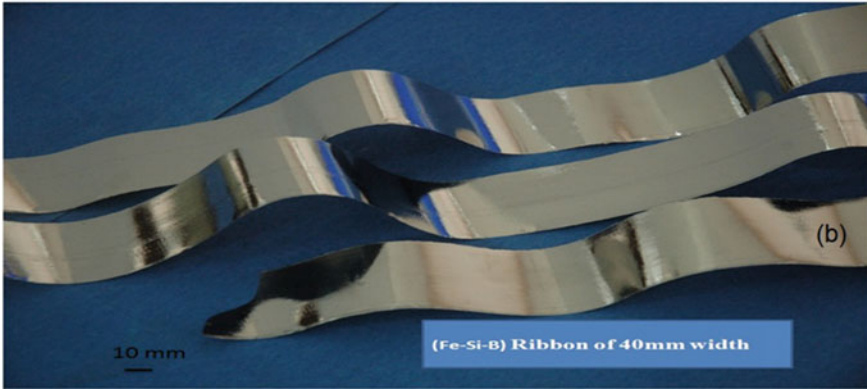
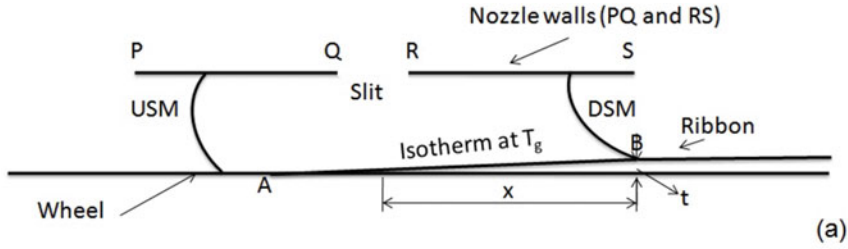


Fig. 1 a Schematic of ribbon formation during PFMS process, b sample ribbon (Fe-Si-B)

Schlichting [14] stated that there exists both laminar and turbulent flows for $2 \times 10^5 < Re < 6 \times 10^5$, where 2×10^5 is the subcritical Reynolds number. Ozisik [11] affirmed that the flow transforms within the boundary layer from laminar to turbulent when the Reynolds number is above 2×10^5 . However, it is difficult to find the Reynolds number in the puddle, as the properties of the melt changes rapidly. Hence, an equation to predict the thickness of thermal boundary layer can be employed to calculate the Reynolds number (Re). The following Eq. (1) is obtained from the equations for thickness of velocity and thermal boundary layer for $Re < 5 \times 10^5$ [8].

$$Re = \left[\frac{\delta_{Tx} Pr^{0.333}}{5x} \right]^2 \tag{1}$$

where δ_{Tx} is the thickness of thermal boundary layer and x is the position on the wheel in the direction of rotation. Thickness of the ribbon is taken as the thickness of the thermal boundary layer δ_{Tx} and x as 5 mm, as the nozzle walls (Fig. 1a PQ and RS) are of 5 mm each. Pr is the Prandtl number, defined as the ratio of molecular diffusivity of momentum to molecular diffusivity of heat and is given by.

$$Pr = \frac{\mu(T)C_p}{k} \tag{2}$$

Table 1 Experiments conducted using Fe_{73.5}Si_{13.5}B₉Nb₃Cu₁ alloy

Expt. no.	Pressure (kPa)	Temp (°C)	Wheel speed (m/s)	Slit length and width (mm × mm)	Gap (mm)	Material weight (g)
1	13.78	1100	18.9	50 × 0.5	0.3	150
2	15.51	1100	18.9	50 × 0.5	0.3	150
3	17.23	1100	18.9	50 × 0.5	0.3	150
4	18.96	1100	18.9	50 × 0.5	0.3	150
5	20.68	1100	18.9	50 × 0.5	0.3	130
6	13.78	1100	25.14	50 × 0.5	0.3	128
7	13.78	1125	25.14	50 × 0.5	0.3	150
8	13.78	1150	25.14	50 × 0.5	0.3	150
9	13.78	1175	25.14	50 × 0.5	0.3	150
10	13.78	1200	25.14	50 × 0.5	0.3	140
11	13.78	1100	18.9	50 × 0.5	0.3	170
12	13.78	1100	20.43	50 × 0.5	0.3	150
13	13.78	1100	22.05	50 × 0.5	0.3	130
14	13.78	1100	23.57	50 × 0.5	0.3	140
15	13.78	1100	25.14	50 × 0.5	0.3	145
16	13.78	1100	22.05	50 × 0.3	0.32	150
17	13.78	1100	22.05	50 × 0.4	0.32	150
18	13.78	1100	22.05	50 × 0.5	0.32	140
19	13.78	1100	22.05	50 × 0.6	0.32	140
20	13.78	1100	22.05	50 × 0.7	0.32	

The show the change in the respective parameter values keeping the rest constant

where C_p is the specific heat, k is the thermal conductivity and $\mu(T)$ is the viscosity at T_g of the alloy (Table 2).

To generalize the phenomenon, the dimensional quantities are to be represented in non-dimensional form. This helps to use the information obtained in the present study for any material and process parameter conditions [5]. All the critical process

Table 2 Material properties

Designation	Parameters	Values
ρ	Density	7180 kgm ⁻³
C_p	Specific heat	544 Jkg ⁻¹ K ⁻¹
k	Thermal conductivity	8.99 W/mK
μ	Viscosity	$\mu(T)$
σ	Surface tension	1.2 N/m
T_g	Glass transition temperature	873 K

parameters, properties of the material, heat transfer parameters and the resulting ribbon dimensional parameters are listed, and the dimensional analysis is applied. The non-dimensional groups derived for the PFMS process using Buckingham π theorem are as given below:

$$\frac{t}{G} = \emptyset \left[\frac{\rho P G^2}{\mu^2}, \frac{\mu C_p}{k}, \frac{\rho U G}{\mu}, \frac{h G}{k}, \frac{w}{G}, \frac{G^2 \rho^2 k T}{\mu^3}, \frac{R_a}{G} \right] \quad (3)$$

Where \emptyset is a function determined experimentally. The groups: $\left[\frac{\rho P G^2}{\mu^2} \right]$, $\left[\frac{\rho U G}{\mu} \right]$, $\left[\frac{w}{G} \right]$ and $\left[\frac{G^2 \rho^2 k T}{\mu^3} \right]$ represent non-dimensional form of pressure, wheel speed, slit width and temperature, respectively. Whereas the groups $\left[\frac{t}{G} \right]$ and $\left[\frac{R_a}{G} \right]$ represent non-dimensional thickness and surface roughness of the ribbon. Group $\frac{\mu C_p}{k}$ represents Prandtl number and $\left[\frac{h G}{k} \right]$ represents Nusselt's number.

3.1 Effect of Process Parameters on the Quality of the Ribbons

The ribbons obtained during the experiments using Finemet alloy at various process conditions show topographies of streak, wavy, dimple and polished. Ribbon obtained is made into 20 equal parts, and the measurement of thickness and roughness is performed on each sample. The error bars shown (Figs. 2, 3, 4 and 5) are 5% for thickness and 3% for surface roughness. Roughness measured on the wheel side for all the ribbons is less than 0.8 μm . Hence, the comparison of roughness as a measure of quality at various process conditions was performed on the airside.

Wheel Speed. Figure 2a–d shows ribbons obtained by varying the wheel speed from 18.9 m/s to 25.1 m/s and the corresponding roughness variations, respectively. Other

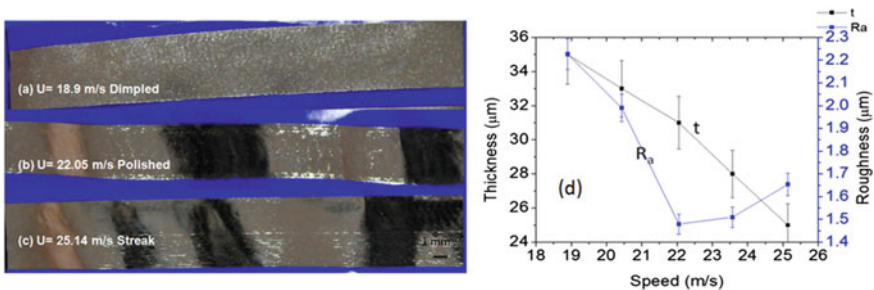


Fig. 2 Ribbons obtained at wheel speeds: **a** 18.9 m/s, **b** 22.05 m/s, **c** 25.14 m/s, **d** effect of speed on thickness and surface roughness

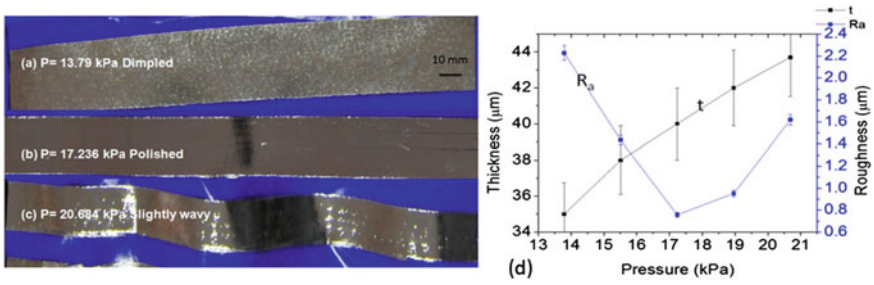


Fig. 3 Ribbons obtained at ejection pressures **a** 13.79 kPa **b** 17.23 kPa **c** 20.68 kPa **d** surface roughness at various ejection pressures

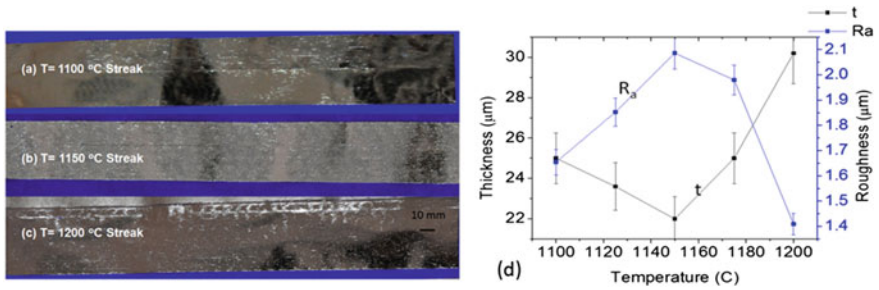


Fig. 4 Ribbons obtained at ejection temperatures **a** 1100 °C **b** 1150 °C **c** 1200 °C **d** surface roughness at various ejection temperatures

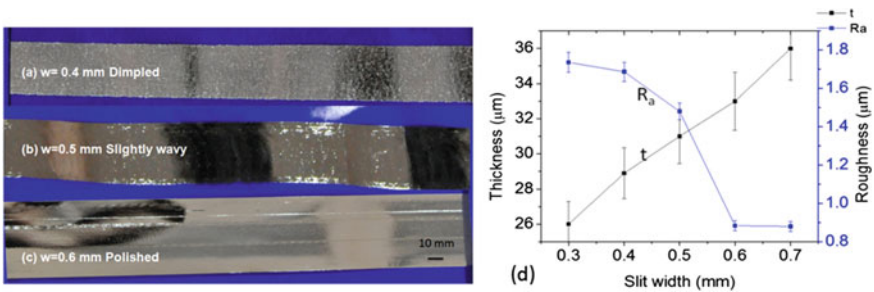


Fig. 5 Ribbons obtained at nozzle-slit width **a** 0.4 mm **b** 0.5 mm **c** 0.6 mm **d** surface roughness at various slit width

process conditions were kept at $P = 13.78$ kPa, $T = 1100^\circ\text{C}$, $G = 0.3$ mm and $w = 0.5$ mm. Dimpled, polished and streak patterns were observed for lower, medium and higher wheel speeds, respectively. Carpenter and Steen [3] predicted that the dimpled pattern was due to non-uniform heat transfer between the wheel and the melt at the meniscus side while streak pattern was due to non-contact of the melt with the wheel at higher speeds.

In the present experiments, the quality of the ribbons is compared using the Reynolds number (Re) and surface roughness. The value of Re calculated using Eq. (1) is in the range 1.5×10^5 – 3×10^5 and shows interesting comparison with roughness as discussed below. With increase in wheel speed from 18.9–22 m/s, the value of Reynolds number is less than 2×10^5 and roughness decreased from 2.2–1.45 μm . With further increase in speed to 25.1 m/s, Reynolds number increased above 2×10^5 and the surface roughness increased to 1.65 μm . The ribbon with polished surface obtained at wheel speed of 22.05 m/s exhibits lowest surface roughness of 1.45 μm for Re nearly 2×10^5 .

The thickness and surface roughness in the dimensional form for various wheel speeds (Fig. 2d) are as given below.

$$t = 22.78 + 2.33U - 0.089 U^2 \quad (4a)$$

$$R_a = 1.47 + 1.117 U - 0.095 U^2 + 0.002 U^3 \quad (4b)$$

The thickness and surface roughness derived in the non-dimensional form for various wheel speeds areas are given below.

$$\frac{t}{G} = 114 \left[\frac{\rho G U}{\mu} \right]^{-1.11} \quad (5a)$$

$$\frac{R_a}{G} = 3 \times 10^{-7} \left[\frac{\rho G U}{\mu} \right]^2 + 0.075 \quad (5b)$$

$$\left(\frac{R_a}{G} \right) \left(\frac{t}{G} \right) = 2 \times 10^{-6} \left[\frac{\rho G U}{\mu} \right]^2 - 0.002 \left[\frac{\rho G U}{\mu} \right] + 0.728 \quad (6)$$

Equation (4a) and (4b) are obtained by curve fitting the values for thickness t and surface roughness R_a measured for change in wheel speed U . Equation (5a), (5b) and (6) is obtained, by curve fitting the values for the dimensionless thickness t/G , dimensionless roughness R_a/G and for the ratio $(R_a/G)/(t/G)$ for change in dimensionless speed $[\rho G U/\mu]$. The non-dimensional thickness and wheel speed in Eq. (5a) show inverse proportionality. Equation (5b) shows increase in roughness with wheel speed. However, the value of coefficients in Eq. (6) shows that the roughness decreases with increase in speed and increases with further increase in speed. Figure 2d obtained from the experimental results also shows the similar trend for dimensional thickness and roughness with increase in wheel speeds. Thickness decreases with wheel speed due to faster melt removal rates as increase in Reynold's number means increase in flow velocity. Wheel speed and flow velocity if balance at DSM, the ribbon obtained may be of higher quality (Re nearly equal to 2×10^5). However, transitional flow ($\text{Re} > 2 \times 10^5$) amplifies the turbulence in the melt, resulting in increase in surface roughness at higher wheel speeds.

Ejection Pressure Figure 3a–d shows the ribbons obtained by varying the ejection pressure from 13.78 kPa to 20.68 kPa and the corresponding roughness variations, respectively. Other process conditions were kept at $U = 18.9$ m/s, $T = 1100^\circ\text{C}$, $G = 0.3$ mm and $w = 0.5$ mm. Dimpled, polished and wavy ribbons are obtained at lower, medium and higher pressures, respectively. Reynolds number calculated from Eq. (1) is less than 2×10^5 at all the pressures. For increase in pressure from 13.79 to 17.23 kPa, roughness decreased from 2.2 to 0.7 μm and Reynolds number decreased from 1.5×10^5 to 1.1×10^5 . With further increase in pressure to 20.68 kPa, roughness increased to 1.6 μm and Reynolds number further decreased to less than 1×10^5 . As the viscous force increases with higher melt flow rate, Reynolds number decreases with increase in pressure.

The thickness and surface roughness in the dimensional form for various ejection pressures (Fig. 3d) are given below.

$$R_a = 29.62 - 3.239 P + 0.091 P^2 \tag{7a}$$

$$t = 0.1148 + 3.39 P - 0.062 P^2 \tag{7b}$$

The thickness and surface roughness derived in the non-dimensional form for various ejection pressures are given below.

$$\frac{t}{G} = 0.003 \left[\frac{\rho P G^2}{\mu^2} \right]^{0.54} \tag{8a}$$

$$\frac{R_a}{G} = 7 \times 10^{-8} \left[\frac{\rho P G^2}{\mu^2} \right]^2 - 0.001 \left[\frac{\rho P G^2}{\mu^2} \right] + 0.098 \tag{8b}$$

$$t = 0.1148 + 3.39 P - 0.062 P^2 \tag{9}$$

Equations (7a) and (7b) are obtained by curve fitting the values t and R_a measured for change in pressure P . Equations (8a), (8b) and Eq. 9 are obtained by curve fitting the values for the ratios t/G , R_a/G and $(R_a/G)/(t/G)$ for change in dimensionless pressure $[\rho P G^2/\mu^2]$. The non-dimensional thickness is proportional to the dimensionless pressure (Eq. 8a) and increases with increase in pressure. However, the surface roughness (Eq. 8b) initially decreases and the positive intercept shows increase in its value with further increase in pressure. This increase in surface roughness is much higher with increase in thickness with pressure as evident from Eq. (9). Figure 3d obtained from the experimental results shows similar trend for both dimensional thickness and roughness. With increase in pressure, more amount of melt accumulates in the gap and increases the residence time of melt in the puddle leading to increase in thickness. The imbalance in flow velocity and wheel speed at low ejection pressures leads to dimple surface on the free side of the ribbon. However, increase in melt flow with increase in pressure suppresses the uneven surface (dimple) and the ribbon

attains polished topography. For pressures higher than 18.96 kPa, Reynolds number is less than 1×10^5 and the ribbon shows wavy topography due to resistance to flow caused by higher viscous force. This wavy surface increases the surface roughness. Present author [15] has observed from the numerical analysis that, higher pressures at lower wheel speeds cause puddle vibration and forms wavy topography, which is suppressed by thinner melts obtained at higher ejection temperatures. However, power consumption increases and more cooling rate is required for higher superheats. Hence, moderate ejection pressures employed at lower superheats (Re near to 2×10^5) may result in higher quality ribbon.

Ejection Temperature. Figure 4a–d shows ribbons and surface roughness variations with change in ejection temperature from 1100 to 1200°C. Other process conditions were kept at $U = 25.14$ m/s, $T = 1100^\circ\text{C}$, $G = 0.3$ mm and $w = 0.5$ mm. The surface topography of all the ribbons is streak pattern. The thickness and surface roughness in the dimensional form for various ejection temperatures (Fig. 4d) are given.

$$R_a = -288.43 + 0.507 T - 2.21 \times 10^{-4} T^2 \quad (10a)$$

$$t = 2658.7 - 4.63T + 0.002 T^2 \quad (10b)$$

The thickness and surface roughness derived in the non-dimensional form for various ejection temperatures are given below.

$$\frac{t}{G} = 13.58 - 5 \times 10^{-7} \left[\frac{G^2 \rho^2 k T}{\mu^3} \right] \quad (11a)$$

$$\frac{R_a}{G} = 5 \times 10^{-8} \left[\frac{G^2 \rho^2 k T}{\mu^3} \right] - 1.435 \quad (11b)$$

$$t = 2658.7 - 4.63T + 0.002 T^2 \quad (12)$$

Equations (10a) and (10b) are obtained by curve fitting the values t , R_a measured for change in melt ejection temperature T . Equation (11a) and (11b) and Eq. (12) are obtained, by curve fitting the non-dimensional terms t/G , R_a/G and $(R_a/G)/(t/G)$ for change in non-dimensional temperature $[G^2 \rho^2 k T / \mu^3]$. Thickness initially decreased and then increased with temperature (Fig. 4d). However, the surface roughness increased initially and then subsequently decreased with further increase in temperature. Equations (11a), (11b) and Eq. (12) show the similar trend for non-dimensional thickness and roughness with increase in temperature.

Reynolds number obtained at various temperatures is higher than 2×10^5 . But it is interesting to observe that the value of Re is initially increased from 3×10^5 to 3.8×10^5 with increase in temperature from 1100 to 1150 °C and then decreased to nearly 2×10^5 at 1200 °C at which the lowest surface roughness of the ribbons is observed. Decrease in viscosity with increase in temperature increases the flow ability of melt and hence increases the Reynolds number and decreases the thickness.

With further increase in temperature, decrease in viscosity leads to spread of melt on the wheel surface causing bigger puddles. This increases the residence time of melt in the puddle and increases the thickness. However, the increase in thickness reduces the flow velocity of melt and hence reduces the Reynolds number. As the value is near to the subcritical value, surface roughness is relatively less.

Ribbons obtained at very high superheats observed to possess dimple pattern due to air entrainment [13, 16]. However, all the ribbons obtained during the present set of experiments show streak pattern. The reason for streak pattern may be the higher wheel speed (25 m/s) selected in all the experiments as on the other hand, the ribbon obtained at 22 m/s and 1100 °C (Fig. 2b) is of polished surface. It infers that the wheel speed is instrumental in obtaining quality ribbon, and the influence of temperature is negligible at higher wheel speeds.

Nozzle-slit width. Figure 5a–d shows ribbons obtained and the surface roughness by varying the nozzle-slit width from 0.3 mm to 0.7 mm. Other process conditions were kept at $U = 22.05$ m/s, $T = 1100^\circ\text{C}$, $G = 0.32$ mm and $P = 13.78$ kPa. Dimple, slightly wavy and polished topographies are observed with low, medium and larger slit width, respectively.

The thickness and surface roughness in the dimensional form for various slit widths (w) (Fig. 5d) are given below.

$$R_a = 0.0938 + 9.535 w - 13.66 w^2 \tag{13a}$$

$$t = 19.1 + 23.38 w + 0.71 w^2 \tag{13b}$$

The thickness and surface roughness derived in the non-dimensional form for various slit widths are given below.

$$\frac{t}{G} = 0.024 \left[\frac{w}{G} \right] + 0.059 \tag{14a}$$

$$\frac{R_a}{G} = 0.006 \left[\frac{w}{G} \right]^3 - 0.038 \left[\frac{w}{G} \right]^2 + 0.44 \left[\frac{w}{G} \right] - 0.014 \tag{14b}$$

$$\left(\frac{R_a}{G} \right) / \left(\frac{t}{G} \right) = 0.057 \left[\frac{w}{G} \right]^3 - 0.268 \left[\frac{w}{G} \right]^2 + 0.36 \left[\frac{w}{G} \right] - 0.082 \tag{15}$$

Equation 13a and 13b is obtained by curve fitting the values t , R_a measured for change in slit width w . Equations (14a), (14b) and (15) are obtained, by curve fitting the values for the non-dimensional terms t/G , R_a/G and $(R_a/G)/(t/G)$ for change in non-dimensional slit width $[w/G]$. Increase in slit width increases the thickness and decreases the surface roughness as interpreted using Equations (14a), (14b) and (15). Similar trend is observed for dimensional thickness and roughness as shown in Fig. 5d. Reynolds number calculated from Eq. (1), for $w = 0.3$ mm to

0.7 mm decreased from 2.7×10^5 to 1.4×10^5 . This is because with increase in slit width the amount of melt flow increases resulting in bigger melt puddle. Hence, the puddle supplies more material and the residence time of melt increases in the puddle, resulting in thicker ribbons. With increase in thickness, the irregularities on the surface are suppressed decreasing the roughness. Of the two big nozzle-slit dimension, 0.6 mm is preferred as the roughness is nearly same but the thickness is much higher for nozzle with slit width of 0.7 mm. The Reynolds number for the nozzle with $w = 0.6$ mm is within the limit of $1.5 \times 10^5 - 2 \times 10^5$ resulting polished surface.

3.2 X-Ray Diffraction Analysis

The melt in contact with the cooling wheel freezes at the glass transition temperature T_g of the alloy. The material near to the wheel cools to lower values due to the no slip boundary at the melt-wheel contact. The cooling effect is much higher near the wheel and decreases with the distance away from the cooling surface. The isotherm of T_g grows from point A to B as shown in Fig. 6. Hence, at point B, there exists a temperature gradient across the thickness of the ribbon. The difference in temperature across the ribbon decreases with decrease in thickness. Furthermore, the projections due to roughness (Fig. 6b) behave as extended surface and enhance the rate of heat transfer leading to difference in temperature on the surface. Hence, thickness and roughness cause temperature gradients across and on the surface of the ribbon, respectively. This gradient in turn defines the amorphous or crystalline nature of the ribbon on the free/airside. Figure 6c shows the roughness visible on the ribbon surface.

Figure 7 presents the XRD analysis performed on both sides of the ribbons. Wheel side represents the contact side of the ribbon with the wheel, and airside represents the

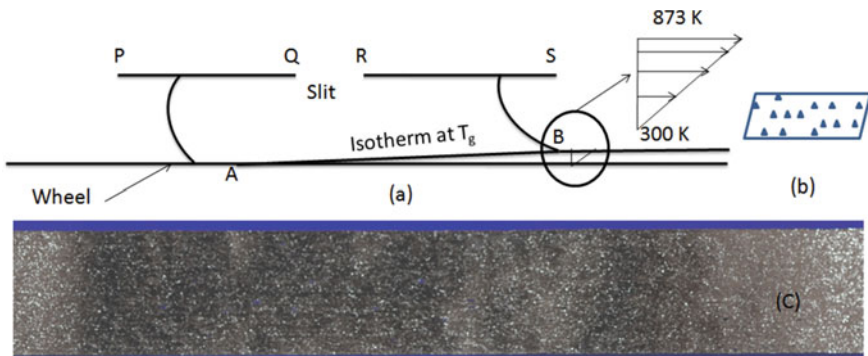


Fig. 6 **a** Schematic of temperature gradient across the ribbon thickness, **b** schematic of surface with roughness, **c** ribbon with high roughness

free side of the ribbon exposed to atmosphere. The wheel side surface of the ribbons shows amorphous nature by a broad hump between 40° and 50° diffraction angle and also show low roughness ($<1 \mu\text{m}$), for all the process conditions. The temperature of the melt in contact with the wheel will always be at the lowest value. Hence, the nature of the ribbon on the wheel side is amorphous for all the process conditions. However, iron peaks on the airside show crystalline nature. The crystalline/amorphous nature on the airside depends on the thickness and roughness of the ribbon. With increase in pressure from 13.78 to 20.68 kPa, both thickness and roughness increased leading to crystalline ribbons (Fig. 7a). For moderate pressures 17.23 kPa, even though roughness is less, higher thickness resulted into crystalline ribbon. Hence, we can infer that, to obtain an amorphous ribbon, lower ejection pressures are sufficient. With increase in wheel speed, even though there is a decrease in thickness, higher surface roughness resulted in to crystalline nature (Fig. 7b). With increase in slit width from 0.3 mm to 0.7 mm, although roughness decreased, increase in thickness and the temperature gradient across the ribbon led to non-amorphous nature on the surface (Fig. 7c).

It was observed by few investigators that the wheel temperature increases during planar flow melt spinning process [6] and wheel may also expands at high temperatures [18]. Present author [17] has observed an increase in wheel temperature leading to crystalline ribbons after a period of casting time. Further, wheel has to absorb more amount of heat with increase in ejection temperature. The effect of temperature on thickness and roughness of the ribbons is opposite. Lowest thickness obtained at 1150°C resulted in to amorphous nature suppressing the effect of roughness on the surface. Hence, super heats less than 100°C are preferred to obtain amorphous nature on the ribbon surface. Hence, we can infer that the temperature gradient across the ribbon and on the surface of the ribbon exists and is the reason for the ribbon being amorphous on the wheel side and crystalline on the free side.

4 Conclusions

Non-dimensional groups derived for the process help to estimate the change in thickness and surface roughness for any change in process parameters. During rapid solidification, the thickness of the ribbon is at the thermal boundary layer formed at the glass transition temperature of the alloy. Amorphous structure depends on the thickness of the ribbon. Hence, Reynolds number calculated from the equation for thermal boundary layer thickness is used for the parametric analysis of the ribbon quality. The inferences drawn are as follows:

- Polished surface topography is observed for $1 \times 10^5 < \text{Re} < 2 \times 10^5$ at the intersection point of melt, ribbon and downstream meniscus.
- Wavy surface is observed for $\text{Re} < 1 \times 10^5$ and streak or dimple topography for $\text{Re} > 2 \times 10^5$

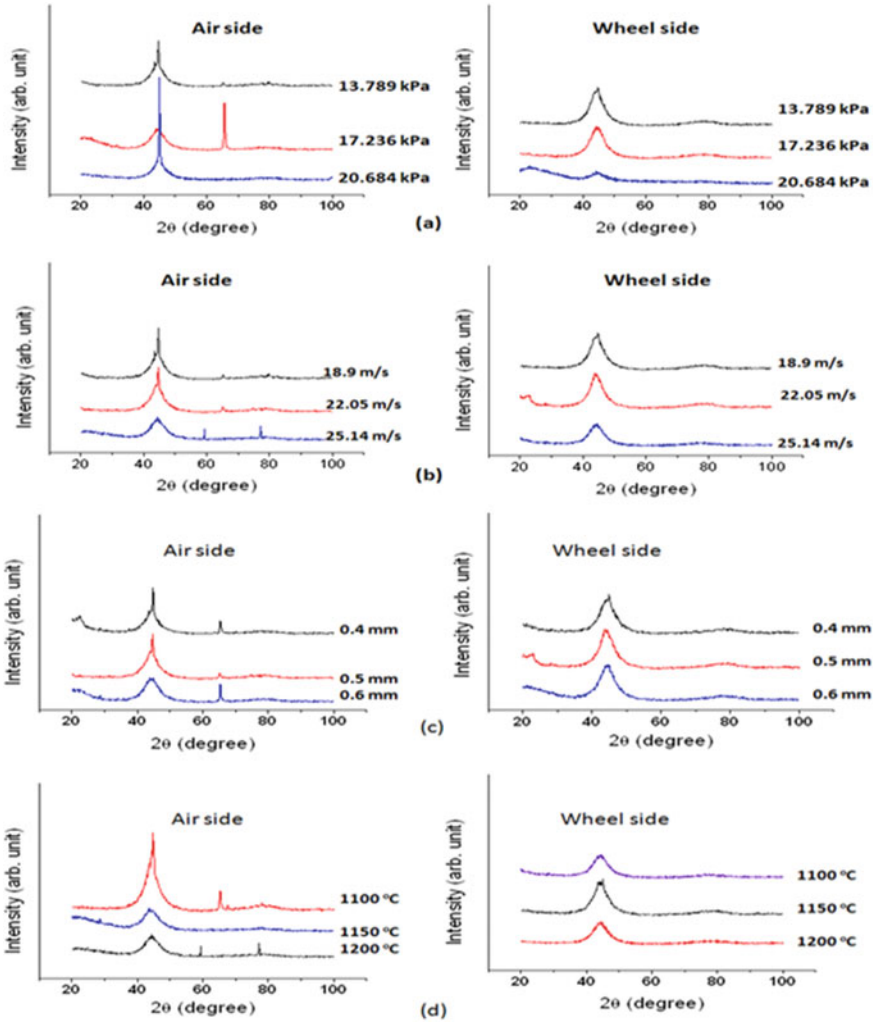


Fig. 7 XRD pattern of the ribbons at various, **a** ejection pressures, **b** wheel speeds, **c** nozzle-slit width, **d** ejection temperature [23].

- Nozzles with larger slit width produced polished ribbons due to unrestricted flow leading to smooth surface on the free side.
- Wheel speed dominates the effect of temperature on the ribbon topography.
- Surface roughness on the wheel side is less than 1 μm for all the ribbons, while varied on the airside with process conditions.
- Polished ribbons show lowest surface roughness on airside.
- Roughness enhances the heat transfer rate on the airside leading to local crystallization.

- Low temperatures near the wheel surface and a gradient across the ribbon result into amorphous and crystalline structure, respectively. Maintaining the wheel at lower temperatures may reduce the crystalline structure on the airside.

Acknowledgements The work is an extension of the research work performed by the author at Defence Metallurgical Research Laboratory (DMRL), Hyderabad (2011–14). The author is thankful to the organization for permitting to perform the research work.

Appendix A

As the properties of FINEMET are not available, the properties of similar alloy (Fe-Si-B) available in the literature (2009) taken for the calculations are as given below.

References

1. Byrne CJ, Theisen EA, Reed B, Steen PH (2006) Capillary puddle vibrations linked to casting-defect formation in planar-flow melt spinning. *Metll. Meterl. Trans. B (37B)*, 445–456 (2006).
2. Byrne CJ (2007) Planar-flow melt spinning: process stability and microstructure control, PhD dissertation, Cornell University
3. Carpenter JK, Steen PH (1992) Planar flow spin casting of molten metals process behavior. *J Mater Sci* 27:215–225
4. Cox BL, Steen PH (2013) Herringbone defect formation in planar-flow melt spinning. *J Mater Proc Tech* 213:1743–1752
5. Ede AJ (1967) An introduction to heat transfer principles and calculations, Int. Pergamon Press, London, pp 9–14
6. Karpe B, Kosec B, Bizjak M (2011) Modeling of heat transfer in the cooling wheel in the melt-spinning process. *J Achiev Mater Manuf Engg* 46:88–94
7. Nakagawa K, Kanadani T, Mori Y, Ishii Y (2011) The effect of jetting temperature on the fabrication of rapidly solidified Fe-Si-B systems alloys using single-roller melt spinning mater. *Trans* 52(2):196–200
8. Kothandaraman CP, Subramanyan S (2008) Heat and mass transfer data book, edn 6. New Age, New Delhi
9. Liu H, Chen W, Qiu S, Liu G (2009) Numerical simulation of initial development of fluid flow and heat transfer in planar flow casting process. *Metall Trans B (40B)*:411–429
10. Matsuki K, Kogiku F, Morito N (1998) Influence of surface roughness on magnetic properties of Fe-Si-B amorphous alloy. *IEEE Trans on Magn* 34(4):1180–1182
11. Ozisik MN (1985) Heat transfer a basic approach int. ed., McGraw-Hill, Singapore, pp 370–372
12. Praisner TJ, JSJ Chen, Tseng AA (1994) An experimental study of process behavior in planar flow melt spinning. *Metl Mater Trans B* 26B:1995–1996
13. Seino R, Yuichi S (2014) Observation of melt puddle behavior in planar flow casting in air. *J Alloy Comps* 586:5150–5152
14. Hermann S (1979) Boundary-layer theory int. ed., Mc-Graw Hill Inc., edn 4, 142–143
15. Sowjanya M, Reddy KKT (2014a) Wavy ribbon formation during planar flow melt spinning process—a 3D CFD analysis. In: 10th international conference on heat transfer, fluid mechanics and thermodynamics, Florida, 14–16

16. Sowjanya M, Reddy KKT, Srivastha B, Majumdar B (2014b) Simulation of initial ribbon formation during planar flow melt spinning process. *Appl Mech Mater* 446–447:352–355
17. Sowjanya M, Reddy KKT (2014c) Cooling wheel features and amorphous ribbon formation during planar flow melt spinning process. *J Mater Proc Tech* 214:1861–1870
18. Sundararajan A, Thomas BG (2008) Heat transfer during melt spinning of Al-7%Si alloy on a Cu-Be wheel. *TMS The Minerals Met Mat Soc*, pp 793–810
19. Szewieczek D, Baron A (2004) Electrochemical corrosion properties of amorphous Fe₇₈ Si₁₃ B₉ alloy. *J Mater Proc Tech* 157–158:442–445
20. Szewieczek D, Baron A (2005) Electrochemical corrosion and its influence on magnetic properties of Fe_{75.5} Si_{13.5} B₉Nb₃Cu₁ alloy. *J Mater Proc Tech* 164–165:940–946
21. Tiberto P, Stantero A, Baicco M, Matko I, Duhaj P (1996) Formation of nano-crystals in amorphous Fe_{73.5} Nb₃ Cu₁ Si_{13.5} B₉ ribbons produced with different quenching rate. *J Nanostruc Mater* 7(6):619–628
22. Chung-Yung W, Kuan-Ju L, Vheng Y-T, Huang C-K, Pan C-N, Li W-C, Chiang L-K, Yeh C-N, Fong S-C (2014) Development of amorphous ribbon manufacturing technology. *China Steel Tech Rep No* 27:28–42
23. Madireddi S (2020) Effect of heat transfer between melt puddle and cooling wheel on amorphous ribbon formation. *Eng Sci Technol Int J* 23(5):1162–1170